Available online at www.sciencedirect.com
ScienceDirect
Catalysis Today 131 (2008) 255–261
CATALYSIS TODAY
www.elsevier.com/locate/cattod

Alumina-supported cobalt-molybdenum catalyst for slurry phase Fischer–Tropsch synthesis

Cyrus G. Cooper, Tuan-Huy Nguyen, Yong-Joon Lee, Kelfin M. Hardiman, Tomasz Safinski, Frank P. Lucien, Adesoji A. Adesina *

Reactor Engineering and Technology Group, School of Chemical Sciences and Engineering, University of New South Wales, NSW 2052, Australia

Available online 3 December 2007

Abstract

An evaluative investigation of the Fischer–Tropsch performance of two catalysts (20%Co/Al_2O_3 and 10%Co:10%Mo/Al_2O_3) has been carried out in a slurry reactor at 2 MPa and 220–260 °C. The addition of Mo to the Co-catalyst significantly increased the acid-site strength suggesting strong electron withdrawing character in the Co-Mo catalyst. Analysis of steady-state rate data however, indicates that the FT reaction proceeds via a similar mechanism on both catalysts (carbide mechanism with hydrogenation of surface precursors as the rate-determining step). Although chain growth, α, on both catalysts were comparable ($\alpha \cong 0.6$), stronger CH_2 adsorption on the Co-Mo catalyst and lower surface concentration of hydrogen adatoms as a result of increased acid-site strength was responsible for the lower individual hydrocarbons production rate compared to the Co catalyst. The activation energy, E, for Co (96.6 kJ mol^{-1}), is also smaller than the estimate for the Co-Mo catalyst (112 kJ mol^{-1}). Transient hydrocarbon rate profiles on each catalyst are indicative of first-order processes, however the associated surface time constants are higher for alkanes than alkenes on individual catalysts. Even so, for each homologous class, surface time constants for paraffins are greater for Co-Mo than Co, indicative that the adsorption of CH_2 species on the Co-Mo surface is stronger than on the monometallic Co catalyst.

Keywords: Fischer–Tropsch synthesis; Bimetallic catalyst; FT kinetics; Co-Mo oxide; Slurry reactor

1. Introduction

Depleting resources and a dramatic increase in price of crude oil has encouraged renewed interest in the development of efficient Gas-to-Liquid (GTL) technology for clean fuels production via Fischer–Tropsch synthesis (FTS). Abundant stranded gas fields as well as coal resources, form reservoirs of synthesis gas feedstock ($CO + H_2$), due to well-established processes such as natural gas steam reforming and coal gasification. While the technology has matured over the past half century, it still struggles to compete with the crude oil market, with catalyst deactivation being a major area of concern.

Research has revealed that supported cobalt is the preferred choice for a commercial catalyst, principally due to its high activity, better selectivity to higher hydrocarbons, and low conversion to CO_2 compared to iron catalysts [1,2]. The focus recently has been on the need for better carbon resilient catalysts than conventional Co catalysts (which suffer from on-line carbon induced deactivation) and improved reactor design and operation for superior alkene selectivity. Pairing traditional FT catalysts (Co, Fe, and Ru) with other metals such as Pt, Mn, and K, has often been used to enhance activity [3–7]. Kogelbauer et al. [2], and Hosseini et al. [8,9] have studied the Ru-promotion of Co/Al_2O_3 catalysts, and its effects on catalyst reducibility and CO hydrogenation activity. Satterfield and Stenger [10], and Bukur et al. [11] have investigated the effects of K- and Cu-promotion of precipitated Fe catalysts, on hydrogenation activity and selectivity. Jacobs et al. [12–16] have carried out extensive work on several noble metals and metal cations promotion of Co (including Pt, Ru, Re, La, Zr, and K), and their effects on the physicochemical properties, and deactivation behavior of the catalysts.

The advantages of improved heat transfer, minimisation of hot-spots and side-reactions, and better catalyst longevity make the slurry reactor more attractive than the fixed bed system [17–23]. Isothermal operability, and longer contact time of reactant gases with catalyst in the slurry reactor, endow it with the potential to produce very high molecular weight hydrocarbons:

* Corresponding author. Tel.: +61 2 9385 5268; fax: +61 2 9385 5966.
E-mail address: a.adesina@unsw.edu.au (A.A. Adesina).

0920-5861/$ – see front matter © 2007 Elsevier B.V. All rights reserved.
doi:10.1016/j.cattod.2007.10.056

these may potentially accumulate as the liquid phase in the reactor. A major drawback though, is the need for product separation from the solid catalyst: both online, as well as of the spent catalyst at the conclusion of a run. Even so, its significant advantages over the fixed and to a lesser extent fluidised bed systems, and a more favourable market for high molecular weight FT products, make the slurry reactor the preferred choice for recent as well as new FT plants. Combined with a supported cobalt catalyst, it forms the latest generation of Sasol's FT reactors for the production of middle distillates and liquid fuels [19,21,24]. Ultimately however, the formulation of a high activity, stable catalyst, is at the heart of the process, if maximal benefits of the slurry reactor are to be enjoyed [25].

Since Mo carbide is known to be active for hydrogenation/dehydrogenation reactions [26,27] and also used as a desulfurisation catalyst [28], the addition of Mo to a Co catalyst for FT reaction should endow it with carbon-resilient attributes especially for sulfur-containing natural gas conversion processes. This constitutes the rationale for this evaluation study of the Co-Mo catalyst. Moreover, ethylene re-adsorption reportedly takes place during FTS [29–32], hence the use of a well-stirred slurry reactor will favour olefin selectivity.

2. Experimental

2.1. Catalyst preparation

Two catalysts (monometallic 20%Co/Al_2O_3, and bimetallic 10%Co-10%Mo/Al_2O_3) were prepared via pH controlled wet impregnation on commercial γ-alumina support (Saint-Gobain Norpro Corporation) using $Co(NO_3)_2.6H_2O$ (Aldrich Chemicals) and $(NH_4)_6Mo_7O_{24}{\cdot}4H_2O$ (Ajax Finechem) as the respective Co and Mo precursors. Accurately weighed amounts of precursor(s) required to make a 20 wt% total metal loading catalyst, were dissolved in ultra pure H_2O to make the precursor solution. The support was ground and sieved to 38–147 μm particle size, before adding to the precursor solution to make the impregnating slurry. Impregnation was carried out at 25 °C for 3 h under constant stirring, constant pH (=2) conditions, using 5 M HNO_3 solution as the pH control. The sub-isoelectric pH impregnation was adopted to create a positively charged support surface, and hence an alike-charged support-impregnating species pair, which would enhance catalyst dispersion, while simultaneously reducing detrimental metal–support interactions [33–36]. Impregnated catalysts were dried in an oven at 120 °C, for 24 h.

The dried catalysts were ground and calcined in flowing dry air, at 400 °C, for 5 h, using a heating rate of 5 °C min^{-1}. The air used was passed through a series of gas purifiers to remove moisture, hydrocarbons and organics. Calcined catalysts were finally ground and sieved to 38–147 μm size before charging 7.5 g (calcined, unreduced basis) in a 1/2 in. diameter stainless steel fixed bed reactor to carry out ex situ activation at 350 °C, for 16 h, with a heating rate of 5 °C min^{-1} in 3:1 H_2:CO mixture, and total GHSV of 1.5 l(STP) g_{cat}^{-1} h^{-1}, with 50% N_2 diluent to dissipate the heat of reaction and minimise generation of hot spots which may lead to coking and catalyst deactivation. High purity research grade H_2 (99.99%), CO (99.97%), and N_2 (99.99%) supplied by Linde Gas were used throughout. Gas flowrates were controlled by Brooks 5850E Series electronic mass flow controllers.

2.2. Catalyst characterisation

The BET surface areas of the calcined catalysts and the γ-alumina support, were obtained from liquid N_2 physisorption at −196 °C, in a Micromeritics AutoChem 2910 unit. Temperature-programmed NH_3 desorption (TPD) was also performed in the same unit after solid pretreatment at 500 °C with H_2 for 3 h. NH_3 (10%NH_3/N_2, Linde Gas) adsorption occurred at 150 °C for 60 min, while desorption was performed in He (99.996%, Linde Gas) flow at heating rates of 10, 15, 20, and 30 °C min^{-1}.

Thermogravimetric analysis of the calcination and reduction behavior of the catalysts was performed using a ThermoCahn TG 2121 system. Temperature-programmed calcination was carried out at 400 °C, for 5 h, with heating rates of 1, 5, and 20 °C min^{-1}, using 55 ml min^{-1} high purity air. Temperature programmed reduction (TPR) was performed up to 700 °C, for 1 h, at 5 °C min^{-1}, in 55 ml min^{-1} of 50% H_2/N_2 mixture. Helium purge (55 ml min^{-1}), and a 3-h initial drying step at 120 °C were incorporated for both calcination and reduction experiments.

2.3. Reaction

Slurry phase Fischer–Tropsch synthesis was performed in a 2 l magnetically-stirred Parr reactor (model 4522). Catalyst activated ex situ in the fixed bed reactor as detailed in Section 2.1, was pneumatically transferred (in flowing N_2) through a ball valve and a dip tube, into the slurry reactor containing 600 g of molten wax, which was also pre-purged with N_2 to eliminate possibility of re-oxidation of the activated catalyst. The dip-tube arrangement prevented catalyst from accumulating on the inside walls of the reactor, above the liquid level, as well as being carried out of the reactor in the gas phase. Paraffin wax from Ajax Finechem with a melting point between 56 and 58 °C, was used as the start-up medium. Following catalyst transfer, the reactor temperature and pressure were increased in N_2 flow to 2 MPa pressure, and the required reaction temperature (220–260 °C) in a two-step isothermal–isobaric process. Syngas flow was then introduced at H_2/CO of 2, with 25% N_2 diluent, and a total GHSV of 3 l(STP) g_{cat}^{-1} h^{-1}. Reactor outlet gases passed through a series of high pressure, hot and cold traps at 80 and 0 °C, respectively. Reactant gases and uncondensed products passed through a back-pressure regulator, located downstream of the cold trap. The flowrate was measured using a soap-film flowmeter, while gas phase products were analyzed on a Shimadzu GC-17A gas chromatograph, using a 30 m GS-Q capillary column and a Flame Ionization Detector (FID).

3. Results and discussion

3.1. Physicochemical attributes

The presence of different oxide phases in the Fischer–Tropsch catalyst and their reducibility is a determinant of the

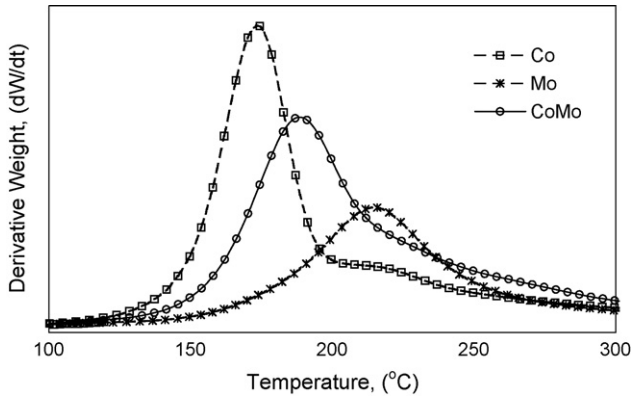

Fig. 1. Derivative weight profiles of temperature-programmed calcinations.

catalyst performance [12], therefore analysis of the thermal spectra for the calcination procedure and H_2 temperature programmed reduction (TPR) will compliment subsequent reaction diagnosis and catalyst evaluation. Fig. 1 shows the thermogravimetric profiles of the two impregnated catalysts (20%Co- and 10%Co-10%Mo/Al_2O_3), and also a monometallic 20%Mo/Al_2O_3 catalyst (prepared for comparative TG analysis), during air calcination at 5 °C min^{-1}. It is evident that decomposition of cobalt nitrate to the Co_3O_4 phase occurred at about 175 °C while the shoulder at 220 °C corresponds to the formation of $CoAl_2O_4$ phase. The Mo catalyst displayed a single decomposition of the ammonium molybdate ($(NH_4)_6Mo_7O_{24}$) precursor to MoO_3, wherein Mo is present in its highest oxidation state as Mo^{6+} in either form. The Co-Mo catalyst is however characterised by a broader oxidative decomposition peak at 190 °C, indicative of the formation of a new intermetallic oxide, $CoMoO_4$ phase [37,38]. Presence of these metal–metal and metal–support interactions are further corroborated by the H_2-TPR spectra (Fig. 2) that were collected directly after the TG-calcination depicted in Fig. 1.

The H_2 TPR spectra in Fig. 2 confirmed the existence of a major Co_3O_4 phase which was reduced in a two-step process from Co_3O_4 (250 °C) → CoO (483 °C) → Co^0 [12]. The last peak at 640 °C may be attributed to the higher temperature reduction of more stable surface $CoAl_2O_4$ species, whilst the initial peaks at 110 and 175 °C represent the removal of chemically bonded water and volatiles from the uncalcined solid. The Mo and Co-Mo profiles are also characterised by

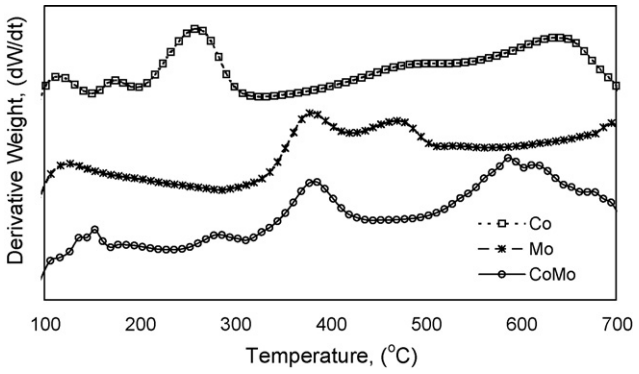

Fig. 2. Derivative weight profiles for temperature-programmed reduction.

multiple peaks below 180 °C due to weight losses from the removal of water, volatiles and ammonium compounds. The primary reduction of MoO_3 is observed at 380 °C, for either catalyst. The gradual reduction of various molybdenum suboxides (e.g. MoO_3, Mo_4O_{11}, MoO_2), from its highest valence of Mo^{6+}, is observed for the monometallic catalyst as a wide plateau extending up to, and beyond the maximum reduction temperature of 700 °C [9,30,39]. The bimetallic Co-Mo catalyst however exhibited significantly different behavior from either of its monometallic counterparts. A complex of overlapping peaks at higher temperatures between 550 and 700 °C, which cannot be explained by a simple convolution of the Co- and Mo-spectra, stipulates the presence of bimetallic ($CoMoO_4$) and potentially bimetallic-support ($MoAl_2O_4$ and $CoAl_2O_4$) interactions. The formation of multiple bulk phase microstructures in composite oxide systems is well known [40], and the existence of Co_3O_4 and $CoMoO_4$ crystallites on the alumina support is consistent with the co-impregnation of cobalt nitrate and ammonium molybdate salts used in this study, as well as the findings of several other researchers [35,39,40]. Accordingly, the BET surface area of the Co catalyst measured as 216 $m^2\ g^{-1}$ (Table 1), is lower than that of the pure alumina support (pretreated in the same manner as the metal catalyst), determined as 278 $m^2\ g^{-1}$. However, most likely due to presence of larger oxide particles in the Co-Mo catalyst, the associated BET area was somewhat smaller at 193 $m^2\ g^{-1}$. NH_3 temperature-programmed desorption (TPD) experiments on both catalysts revealed that the Co-Mo oxide possessed stronger acid sites ($-\Delta H_{desorp} = 48$ kJ mol^{-1} for Co-Mo, c.f. 24 kJ mol^{-1} for Co) due to the higher electron deficiency at the interface between the Co and Mo oxides in the Co-Mo catalyst. The similarity in the acid site concentration, 650 μmol(NH_3) g_{cat}^{-1} is probably a reflection of the identical metal loading used in the two catalysts. The solid-state calcination kinetics data analyses carried out as described in Brown [41], further yielded activation energy values of 115 and 245 kJ mol^{-1} for the Co and Co-Mo oxides, respectively.

3.2. Steady-state reaction runs

Experiments conducted with feed containing H_2:CO ratio of 2:1 at three different temperatures (220–260 °C) and 2 MPa pressure were used to evaluate the FT performance of the two catalysts. To minimize transport effects, a stirrer speed of 700 rpm using a dual 6-blade propeller stirrer, and catalyst particle size of 38–147 μm were employed. Runs were carried out over a 16-h period with on-line GC analysis of the gas phase (C_1–C_8) hydrocarbons. There is a general consensus that the FT

Table 1
Physicochemical properties of Co and Co-Mo catalysts

	Co	Co-Mo
BET surface area ($m^2\ g^{-1}$)	216	193
ΔH_{desorp} NH_3 (kJ mol^{-1})	24	48
Acid-site concentration (μmol g_{cat}^{-1})	650	650
Activation energy, E_A (kJ mol^{-1})	115	245

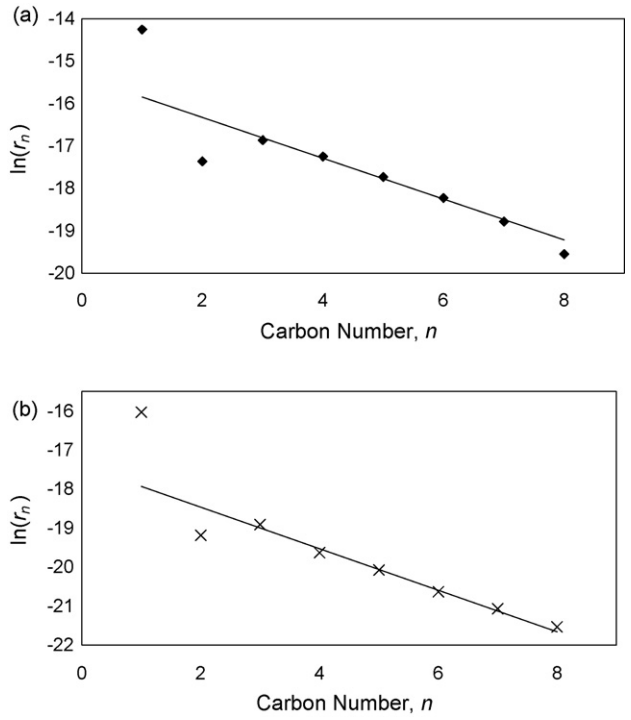

Fig. 3. ASF plots for (a) Co and (b) Co-Mo catalysts at 220 °C.

synthesis is a polymerization reaction, thus, the steady-state hydrocarbon rate data were fitted to the Anderson–Schulz–Flory (ASF) equation [42]

$$r_n = k_{\mathrm{ASF}}(1-\alpha)^2\alpha^{n-1} \quad (1)$$

where r_n is the total production rate for all hydrocarbons with n carbon atoms, α is the chain growth probability, and k_{ASF} is a pseudo-rate constant equal to the CO consumption rate when CO_2 formation is negligible as is the case on Co-based FT catalysts [43]. Fig. 3(a and b) illustrates the ASF plots for the two catalysts at 220 °C, while Table 2 displays the ASF parameters for the catalysts. It is apparent that α has a weak dependency on temperature while the pseudo-rate constant, k_{ASF}, follows Arrhenius behavior with accompanying activation energy, E_{ASF}, values of 97 and 111 kJ mol^{-1} for the Co and Co-Mo catalysts, respectively. The corresponding pre-exponential factors, k^0_{ASF} are 1.8×10^4 and 6.1×10^4 s^{-1}. The magnitudes (>20 kJ mol^{-1}) of these activation energy estimates are consistent with the absence of transport intrusions.

The individual activation energy values for observed product on both catalysts are provided in Table 3. In general, E_{alkanes} are

Table 2
Characteristic ASF parameters

T (°C)	Co		Co-Mo	
	α	k_{ASF} ($\times 10^7$) (mol g_{cat}^{-1} s^{-1})	α	k_{ASF} ($\times 10^7$) (mol g_{cat}^{-1} s^{-1})
220	0.65	9.3	0.58	0.96
240	0.64	33	0.56	2.6
260	0.59	54	0.59	7.4

Table 3
Individual component activation energies, E_{HC}

HC component	H:C ratio	E_{HC} (kJ mol^{-1})	
		Co	Co-Mo
CH_4	4.00	112	116
C_2H_6	3.00	133	135
C_3H_8	2.67	133	143
C_4H_{10}	2.50	113	133
C_5H_{12}	2.40	115	138
C_6H_{14}	2.33	77	128
C_7H_{16}	2.29		113
C_2H_4	2.00	42	29
C_3H_6	2.00	45	64
C_4H_8	2.00	16	66
C_5H_{10}	2.00	17	43
C_6H_{12}	2.00		44
C_7H_{14}	2.00		20

between 100 and 140 kJ mol^{-1} and are about 2–3 times those for the alkenes (20–60 kJ mol^{-1}). Although there is no particular trend in the activation energy variation with respect to carbon number, Fig. 4 shows that for the alkanes, E_{HC} is a function of the H:C ratio in the molecule. The curves for both Co and Co-Mo catalysts are essentially parallel suggesting similarity in the energetics of the surface hydrocarbon-producing reactions. The difference between the two envelopes may be due to the electron withdrawing effect of Mo on the Co center and hence greater energy barrier in the activation of surface species consistent with strong adsorption of CH_x species on the catalytic sites. The sharp turning point in E_{HC} at H:C of about 2.6 is further evidence that the production of higher alkanes (beyond $n \geq 3$) is more energetically facile since the H:C ratio now approaches that of alkenes (H:C = 2). Since the overall reaction rate on each catalyst is characterised by an activation energy value closer to those for the alkanes, the rate-determining step was the termination step involving hydrogenation of surface unsaturated species to alkanes and an indication of relatively low hydrogen adatoms especially on the Co-Mo oxide.

The alkene-to-alkane (olefin-to-paraffin) ratio varies with both temperature and carbon number on both catalysts as depicted in Fig. 5. This behavior may be adequately captured by,

$$\mathrm{ROP}_n = Ab^n \quad (n \geq 1) \quad (2)$$

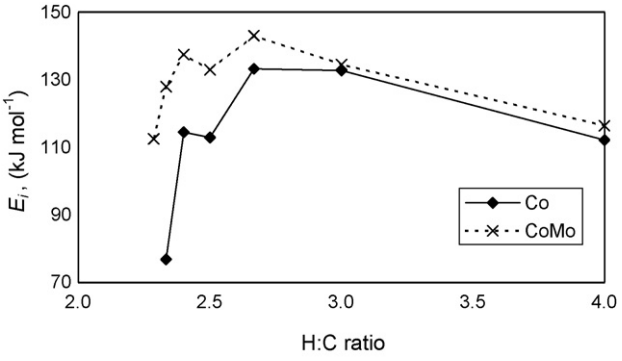

Fig. 4. Dependence of activation energies of paraffins on their H:C ratio.

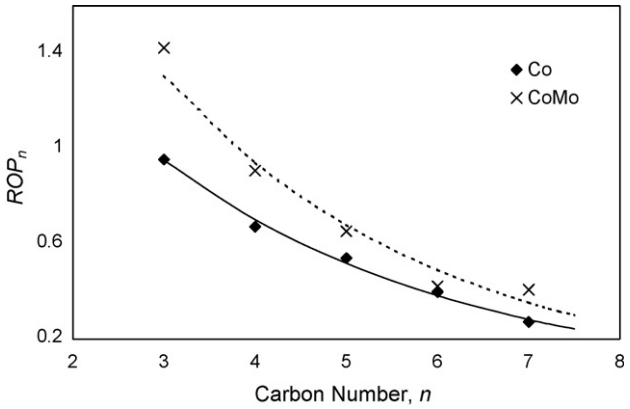

Fig. 5. Ratio of olefin-to-paraffin (ROP_n) trend.

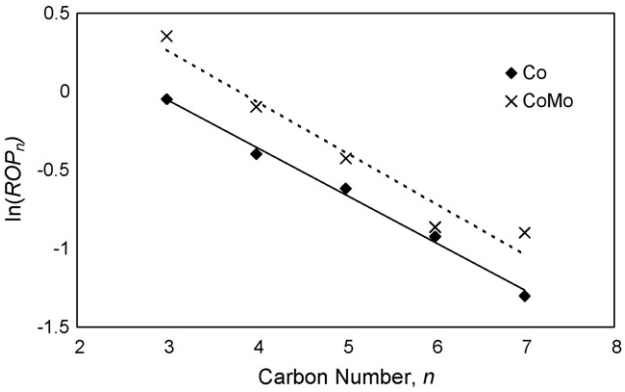

Fig. 6. Plot of ROP_n data in terms of proposed model.

or,

$$\ln(\mathrm{ROP}_n) = \ln(A) + n\ln(b) \tag{3}$$

as demonstrated by the linear plot shown in Fig. 6, where ROP_n is the ratio of the alkene rate to alkane rate for the nth carbon chain. For $n = 1$, Eq. (2) yields

$$r_{\mathrm{CH_2}} = r_{\mathrm{CH_4}} Ab \tag{4}$$

where r_{CH_2} is the production rate of the surface CH_2 monomer for the polymerisation reaction. For a surface rate step, the temperature dependency may be written,

$$r_{\mathrm{CH_2}} = k^0_{\mathrm{CH_2}} \mathrm{e}^{-E_{\mathrm{CH_2}}/RT} \tag{5}$$

where Arrhenius treatment of the data yields, E_{CH_2} for Co and Co-Mo catalysts as 45 and 50 kJ mol^{-1}, respectively, with associated frequency factors, $k^0_{CH_2}$, of 6.4×10^{-2} and 5.5×10^{-2} s^{-1}. The similarity in the activation energy for CH_2 production and those for light alkene formation on both catalysts suggests that the surface propagation rate,

$$n\mathrm{CH_2} \rightarrow (\mathrm{CH_2})_n \tag{6}$$

is barely temperature sensitive and more energetically facile (activation energy for the propagation step is negligible) than the initial step for CH_2 production. This is in agreement with the observation of a weak dependency of α on temperature as

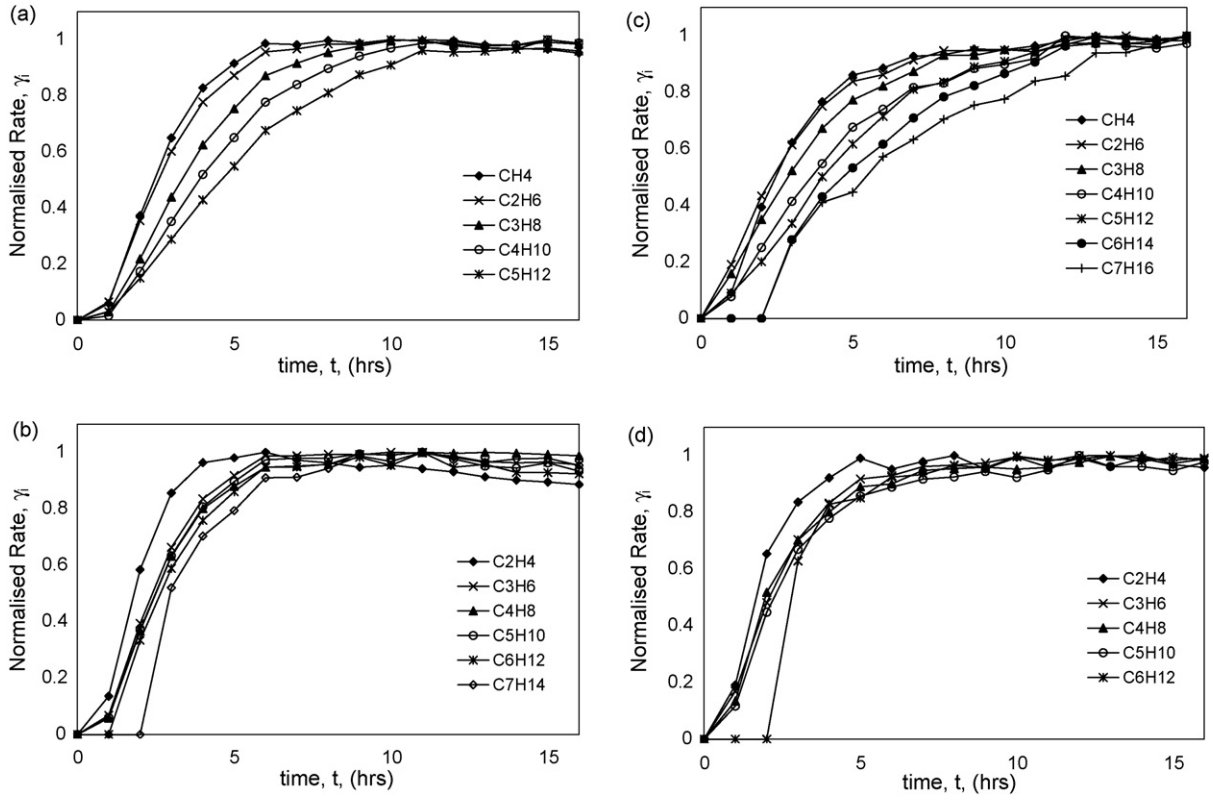

Fig. 7. Transient profiles of paraffins (a and c) and olefins (b and d) for Co (a and b) and Co-Mo (c and d) catalysts, at 220 °C.

seen in this study, given that,

$$\alpha = \frac{r_p}{r_p + r_t} \quad (7)$$

where r_p and r_t are defined as the rates of propagation and termination, respectively. Interestingly, the estimates are practically identical with those implicated in Fig. 4.

3.3. Transient reaction profiles

The transient reaction rate profiles for various hydrocarbons are shown in Fig. 7(a–d) for both alkenes and alkanes, for both catalysts at 220 °C. Since the slurry CSTR was operated under non-reactive thermal steady-state conditions before the introduction of syngas mixture, these response curves are effectively the signals from a step-change change (0% CO to 33.3% CO feed), in syngas composition and hence, a reflection of the reaction dynamics. In particular, the response curves possess the features of a typical first-order process with time-delay. Thus, the normalised transient rate, γ_i, for the ith species, may be written,

$$\gamma_i = 1 - e^{-t'/\beta} \quad (8)$$

where $t' = t - t_d$ with t_d as the time-delay (ca. 1 h), and β_i is the relaxation time constant for component i. It is noteworthy that on each catalyst, alkenes generally rose to their steady state values faster than the corresponding alkanes. Although a detailed dynamic process is not presented here, it is apparent that the relaxation time constant, β, increased with carbon number. Moreover, β values are smaller for alkenes than the alkane with the same carbon number. This is further indication that in the sequence of the surface elementary steps, alkenes are the precursors to alkanes once the monomeric CH_2 species have been formed. Between the two catalysts however, alkane production was more sluggish on the Co-Mo system, consistent with our previous study [44] for fixed bed systems, that Mo addition suppressed alkane formation and hence improved olefin selectivity. This is also in agreement with the ROP_n values for the Co and Co-Mo catalysts in the present investigation. On the other hand, alkenes rose to the steady-state values comparatively faster on the Co-Mo catalyst than on the Co oxide confirming the enhanced alkene selectivity due to the presence of Mo in the bimetallic catalyst.

4. Conclusions

Physicochemical characterisation of the catalysts has confirmed the existence of complex metal–metal and metal–support species. Lower BET area of the bimetallic catalyst suggested larger crystallite size on the Co-Mo catalyst, while NH_3 TPD revealed that addition of Mo results in stronger acid sites, a consequence of the higher electron deficiency at the interface between the Co and Mo species.

Steady-state analysis revealed a weak dependency of α, the chain growth probability, on temperature, while k_{ASF}, the pseudo rate constant derived from the Anderson–Schulz–Flory (ASF) plot follows Arrhenius behavior, with both activation energy, E_{ASF}, and pre-exponential factors, k^0_{ASF}, greater for the bimetallic catalyst. The individual component activation energies of paraffins were 2–3 times those of the corresponding olefins, suggesting olefins as the primary surface products, while greater activation energies on the Co-Mo surface within each homologous series is probably an outcome of the electron withdrawing effect of Mo on the Co center, causing a greater energy barrier. Derivation of the activation energies and frequency factors of the surface methylene species by employing the proposed model for the ratio of olefin-to-paraffin ($ROP_n = Ab^n$), revealed that the surface propagation rate is in fact more facile than the initial monomer production, consistent with our findings of weak temperature dependency of α.

Transient individual component reaction rate profiles depicted first-order response behavior with time delay. The general trend of faster response of the olefins to paraffins, further indicates olefins as the primary products, or precursors to paraffins, while a comparatively more sluggish response of paraffins on the Co-Mo surface confirms the hypothesised benefits of improved alkene selectivity on the bimetallic catalyst.

Acknowledgements

The authors appreciate the financial support of the Australian Research Council. C.G.C. is also a grateful recipient of an Australian Postgraduate Award (APA).

References

[1] S. Hammache, J.G. Goodwin, R. Oukaci, Catal. Today 71 (2002) 361.
[2] A. Kogelbauer, J.J.G. Goodwin, R. Oukaci, J. Catal. 160 (1996) 125.
[3] K. Lee, A. Ishihara, S. Mitsushima, N. Kamiya, K.-i. Ota, Electrochim. Acta 49 (2004) 3479.
[4] L. Bai, H.-W. Xiang, Y.-W. Li, Y.-Z. Han, B. Zhong, Fuel 81 (2002) 1577.
[5] C. Cabet, A.C. Roger, A. Kiennemann, S. Lakamp, G. Pourroy, J. Catal. 173 (1998) 64.
[6] Y. Yang, H. Xiang, R. Zhang, B. Zhong, Y. Li, Catal. Today 106 (2005) 170.
[7] C.-H. Zhang, Y. Yang, B.-T. Teng, T.-Z. Li, H.-Y. Zheng, H.-W. Xiang, Y.-W. Li, J. Catal. 237 (2006) 405.
[8] S.A. Hosseini, A. Taeb, F. Feyzi, Catal. Commun. 6 (2005) 233.
[9] S.A. Hosseini, A. Taeb, F. Feyzi, F. Yaripour, Catal. Commun. 5 (2004) 137.
[10] C.N. Satterfield, H.G. Stenger, Ind. Eng. Chem. Process Des. Dev. 23 (1984) 849.
[11] D.B. Bukur, D. Mukesh, S.A. Patel, Ind. Eng. Chem. Res. 29 (1990) 194.
[12] G. Jacobs, J.A. Chaney, P.M. Patterson, T.K. Das, B.H. Davis, Appl. Catal., A 264 (2004) 203.
[13] G. Jacobs, T.K. Das, P.M. Patterson, J. Li, L. Sanchez, B.H. Davis, Appl. Catal., A 247 (2003) 335.
[14] G. Jacobs, T.K. Das, Y. Zhang, J. Li, G. Racoillet, B.H. Davis, Appl. Catal., A 233 (2002) 263.
[15] G. Jacobs, P.M. Patterson, T.K. Das, M. Luo, B.H. Davis, Appl. Catal., A 270 (2004) 65.
[16] G. Jacobs, P.M. Patterson, Y. Zhang, T. Das, J. Li, B.H. Davis, App. Catal., A 233 (2002) 215.
[17] B. Jager, R. Espinoza, Catal. Today 23 (1995) 17.
[18] A.A. Adesina, App. Catal., A 138 (1996) 345.
[19] R.L. Espinoza, A.P. Steynberg, B. Jager, A.C. Vosloo, Appl. Catal., A 186 (1999) 13.

[20] H. Schulz, Appl. Catal., A 186 (1999) 3.
[21] S.T. Sie, R. Krishna, Appl. Catal., A 186 (1999) 55.
[22] B.H. Davis, Catal. Today 71 (2002) 249.
[23] D.B. Bukur, Ind. Eng. Chem. Res. 44 (2005) 6038.
[24] B. Jager, Development of Fischer–Tropsch reactors, in: AiChE Spring Meeting, New Orleans, 2003.
[25] T.C. Bromfield, A.C. Vosloo, Macromol. Symp. 193 (2003) 29.
[26] K.Y. Park, W.K. Seo, J.S. Lee, Catal. Lett. 11 (1991) 349.
[27] H.C. Woo, K.Y. Park, Y. Kim, G.,L.-S. Nam, J.S. Chung, J.S. Lee, Appl. Catal. 75 (1991) 267.
[28] J.S. Lee, M. Boudart, Appl. Catal. 19 (1985) 207.
[29] P.L. Silveston, R.R. Hudgins, A.A. Adesina, G.S. Ross, J.L. Feimer, Chem. Eng. Sci. 41 (1986) 923.
[30] J.A. Rodriguez, J.Y. Kim, J.C. Hanson, J.L. Brito, Catal. Lett. 82 (2002) 103.
[31] D.B. Bukur, L. Nowicki, X. Lang, Chem. Eng. Sci. 49 (1994) 4615.
[32] T. Komaya, A.T. Bell, J. Catal. 146 (1994) 237.
[33] M. Houalla, C.L. Kibby, L. Petrakis, D.M. Hercules, J. Catal. 83 (1983) 50.
[34] Y.-J. Huang, J.A. Schwarz, Appl. Catal. 32 (1987) 45.
[35] S.L. Chen, H.L. Zhang, J. Hu, C. Contescu, J.A. Schwarz, Appl. Catal. 73 (1991) 289.
[36] K. Inamura, K. Uchikawa, S. Matsuda, Y. Akai, Appl. Surf. Sci. 121–122 (1997) 468.
[37] Y. Okamoto, T. Shimokawa, T. Imanaka, S. Teranishi, J. Catal. 57 (1979) 153.
[38] Y. Okamoto, T. Imanaka, S. Teranishi, J. Catal. 65 (1980) 448.
[39] J.A. Rodriguez, S. Chaturvedi, J.C. Hanson, J. Phys. Chem. B 103 (1999) 770.
[40] H. Chen, A Study of a Co-Mo Bimetallic Catalyst System for Fischer–Tropsch Synthesis, University of New South Wales, Sydney, Australia, 1995.
[41] M.E. Brown, Introduction to Thermal Analysis: Techniques and Applications, Kluwer Academic, Dordrecht, 2001.
[42] R.B. Anderson, The Fischer–Tropsch Synthesis, Academic Press, Orlando, FL, 1984.
[43] A.A. Adesina, J. Catal. 124 (1990) 297.
[44] H. Chen, A.A. Adesina, Appl. Catal., A 112 (1994) 87.